# The effects of low-velocity layer and basin topography on near-field ground motion amplification

Zeyu Lu[1], Jian Wen[1,2], and Feng Hu[1,2] ✉

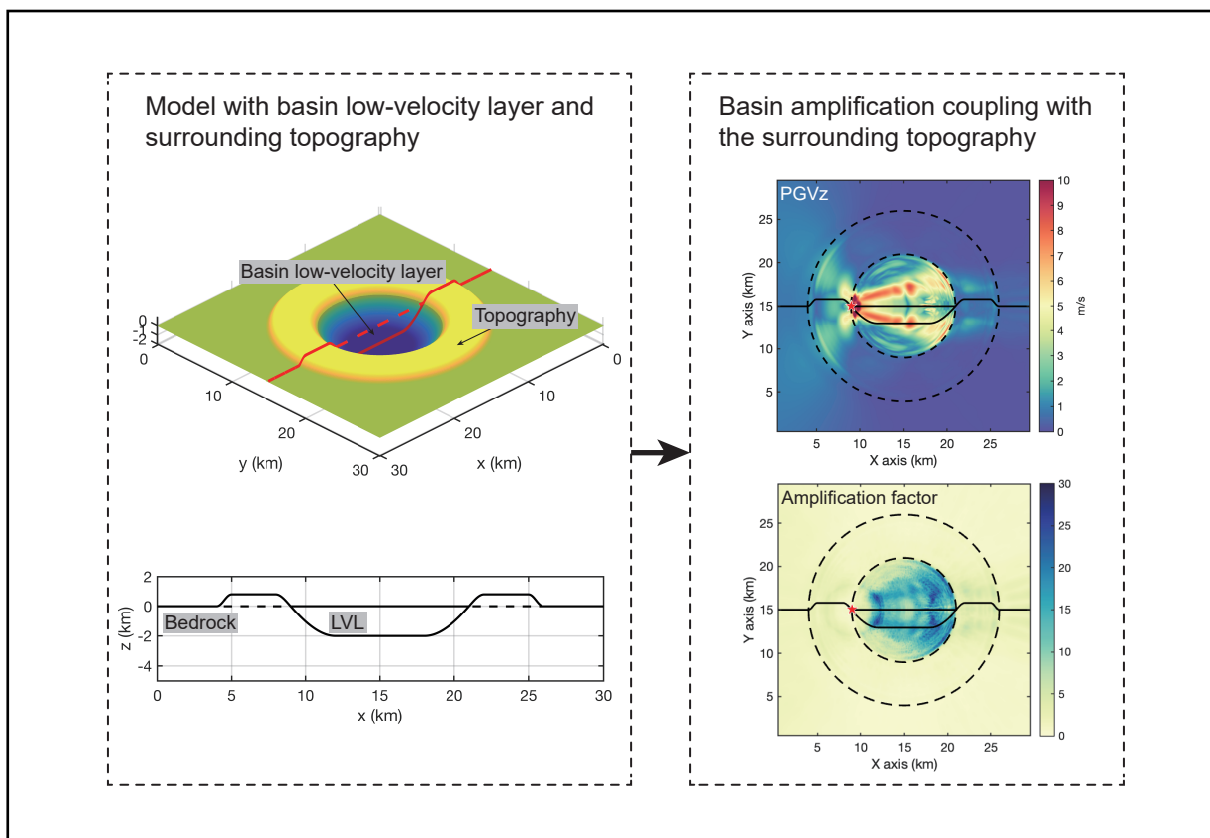*1State Key Laboratory of Precision Geodesy, School of Earth and Space Sciences, University of Science and Technology of China, Hefei 230026, China;*
*2Mengcheng National Geophysical Observatory, University of Science and Technology of China, Mengcheng 233500, China*

✉Correspondence: Feng Hu, E-mail: hufeng07@ustc.edu.cn

## Graphical abstract



*By introducing a basin model that includes both low-velocity layer and topography in earthquake ground motion simulation, the characteristics of ground motion amplification can be acquired.*

## Public summary

■ The effect of the low-velocity layer in contrast with the surrounding mountain topography of a sedimentary basin model is scrutinized by near-field ground motions.

■ Velocity contrast between bedrock and low-velocity layer plays a pivotal role in controlling the amplitude of the ground motion amplification.

■ Amplification caused by the topography mainly spreads along the mountain edge and may interact with the low-velocity

layer to amplify ground motion.

# The effects of low-velocity layer and basin topography on near-field ground motion amplification

Zeyu Lu[1], Jian Wen[1,2], and Feng Hu[1,2] ✉

[1]*State Key Laboratory of Precision Geodesy, School of Earth and Space Sciences, University of Science and Technology of China, Hefei 230026, China;*

[2]*Mengcheng National Geophysical Observatory, University of Science and Technology of China, Mengcheng 233500, China*

✉Correspondence: Feng Hu, E-mail: hufeng07@ustc.edu.cn

**Abstract:** Near-field ground motion amplification in sedimentary basins is widely observed and crucial to earthquake hazard assessment. However, the effects of basin topography coupled with the low-velocity layer (LVL) on ground motion amplification are not fully understood. By constructing 3D basin models with surrounding mountain terrains and performing ground motion simulations, we compare the ground motion characteristics with different basin LVL depths and LVL velocities. The velocity contrast between the LVL and bedrock controls the amplification magnitude. The maximum amplification area in the model changes from the central part to the periphery part of the basin as the velocity contrast decreases and can be greatly influenced by the distance between the source and the basin. The amplification also spreads along the mountain edge circling the basin. Our work sheds light on the distribution of amplification within sedimentary basins surrounded by mountains, revealing that the velocity contrast between the LVL and bedrock plays a pivotal role in controlling the magnitude of amplification.

**Keywords:** low-velocity layer; basin topography; strong ground motion

**CLC number:** P315.3[+]1        **Document code:** A

## 1    Introduction

Near-field ground motion amplification in basin areas is important for earthquake hazard assessment. This is particularly pertinent due to the occurrence of numerous destructive earthquakes in proximity to basins, such as the 1994 Mw 6.7 Northridge earthquake in the Los Angeles Basin area, the 1995 Mw 6.9 Kobe earthquake in the Osaka Basin, and the 2008 Mw 7.9 Wenchuan earthquake and the 2021 Mw 6.0 Luxian earthquake in the Sichuan Basin area[1–5]. The amplified amplitude of ground motion and longer duration of seismograms are the key characteristics in basin areas. However, the effect of the topography of the basin area coupled with the effect of the low-velocity layer in the basin has yet to be fully elucidated.

Previous studies have yielded a wealth of analytical and numerical insights, starting with simpler models such as layered models or simple basin models in homogeneous half-space[6–8]. As the complexity of considered basin geometries or media increases, numerical methods have been introduced to address these challenges. Studies have employed 2-dimensional models, considering configurations like joint of semi-elliptical and rectangle, and half-cosine configurations[9]. Plane-incident waves are frequently applied in these works. Three-dimensional models, such as semi-ellipsoidal, hemispherical, and trapezoidal, have also been used in previous

studies[10–13]. Beyond theoretical models, researchers have conducted ground motion simulations on real basins, such as the Seattle Basin, the Indo-Gangetic (IG) Basin, the Kinburn Basin, the Beijing Basin, the Taipei Basin, and the Sichuan Basin[2,14–22].

Basins are typically enclosed by mountains. The topographic effect also contributes to seismic waveform complexities, which have been known for decades[23–27]. Numerical methods have also been applied to study topographic site effects, although many of them have primarily focused on 2D simulations[28–30]. Some studies have simultaneously considered the effects of topography and velocity structure in assessing seismic ground motion and amplification[30–32]. However, owing to the complexity of real-world velocity structures and topography, assessing seismic responses can be challenging[28,31,33]. Thus, we propose to investigate the contributions of both factors to ground motion amplification within a set-up 3D model.

Among the existing studies, a systematic analysis of basin depth coupled with basin topography within 3D scenarios has been lacking. For instance, depth-dependent wedge-shaped basin models have not been considered. To address this gap, we start with a baseline model, focusing on the sedimentary basin depth and the velocity contrast between the low-velocity layer and the underlying bedrock. To isolate the effect of basin topography in contrast to the low-velocity layer of the

sedimentary basin, we scrutinize the basin amplification effect by comparing a basin model with a homogeneous half-space model. Furthermore, the wedge-shaped basin model is also discussed.

## 2 Models and methods

### 2.1 3D sedimentary basin geometry

We aim to establish a three-dimensional basin model that can be characterized by parameters to conduct near-field seismic ground motion simulation. Ayoubi et al.[9] systematically analyzed the ground motion characteristics of 2D basin models via the finite-element method. They proposed two types of models, semi-elliptical and half-cosine 2D basin models, to perform simulations. We integrate the half-cosine method from Ref. [9] with cubic-spline interpolation to define the basin geometry. The basin area is bounded by encircling mountains. The mathematical expression of the central line curve is given by Eq. (1), which controls the 3D model boundaries in the $x$-axis plane.

$$p(x) = \begin{cases} -d, & |x| \leq a/2; \\ B_{i1}x^3 + B_{i2}x^2 + B_{i3}x + B_{i4}, \\ & a/2 < |x| \leq a+b; \\ h, & a+b < |x| \leq a+b+w; \\ \dfrac{h}{2}\cos\left[\dfrac{\pi}{b}(x-a-b-w)\right] + \dfrac{h}{2}x, \\ & a+b+w < |x| \leq a+2b+w; \\ 0, & |x| \geq a+2b+w; \end{cases} \tag{1}$$

where parameters $a$, $b$, $h$, $d$, and $w$ are the topography and basin geometry constraining parameters, which represent the radius of the basin, the width of the transition area, the height of the mountain around the basin, the depth of the sedimentary basin, and the width of the mountain around the basin, respectively (Table 1). A schematic diagram of the definitions of these parameters is shown in Fig. 1c and 1d. In the model with a fixed depth, by rotating this curve around a central axis to form a three-dimensional surface, the concave portions in the central part of the surface are filled with low-velocity media, forming a low-velocity sedimentary basin (Fig. 1a, 1c). This model is similar to the models of Ayoubi et al.[9] and Qin et al.[11], but includes the mountains around the basin.

We also designed a wedge-shaped basin model. In the wedge-shaped basin model, the model is constructed on the basis of the $x$-direction central line, employing the same interpolation method in the $y$-direction as that used to derive the central axis, forming the entire plane (Fig. 1b, 1d). Similarly, the concave portions in the central part of the surface, which lies below the ground surface, are filled with low-velocity media, forming a sedimentary basin.

### 2.2 Numerical modeling

The ground motion simulations are performed via the CGFD3D (Curved Grid Finite-Difference 3D) code, which applies 3D collocated-grid finite-difference code to solve the velocity–stress equations for the curvilinear grid[34]. In this method, the fourth-order Runge–Kutta scheme is applied to update the wavefield, and the DRP/opt MacCormack scheme provides fourth-order accuracy in space[35]. With a 3D curve grid, the grid can align with the surface topography and avoid spurious diffusion. The code is verified in the work of Zhang et al. by comparison against the generalized reflection/transmission coefficients method (GRTM) and SpecFEM3D code and shows good consistency with the reference solution[34, 36, 37].

In models with a low-velocity layer (LVL), the basin area is filled with low-velocity material with a given depth $d$. In all the models, the shear wave velocity of the bedrock is consistently set at 3000 m/s. All the models assume a Poisson medium to constrain the relationship between P-wave velocity and S-wave velocity. The density for a specific velocity is constrained by the empirical relationship of Brocher[38]. With the range of 1500 m/s $< V_p < $ 8500 m/s, the relationship between $V_p$ and density $\rho$ is described in Eq. (2).

$$\rho\,(\text{g/cm}^3) = 1.6612V_p - 0.4721V_p^2 + 0.0671V_p^3 - 0.0043V_p^4 + 0.000106V_p^5, \tag{2}$$

where $V_s$, $V_p$, and $\rho$ represent the shear wave velocity, compression wave velocity, and the density, respectively.

All the models have a horizontal grid size of 50 m to ensure computational accuracy and reduce numerical dispersion. To reduce the computational burden, the vertical grid size gradually varies from 50 m near the surface to 100 m in deeper regions. The simulation is performed using a time interval of 0.003 s. Among all groups of simulations, the lowest S-wave velocity is 1500 m/s. Considering a minimum PPW

**Table 1.** Basin model parameter definitions and baseline values.

| Parameter | Definition | Baseline value |
|---|---|---|
| $a$ | Radius of the basin | 6000 m |
| $b$ | Width of the transition area | 1000 m |
| $h$ | Height of the mountain around the basin | 800 m |
| $d$ | Depth of the fixed-depth flat basin model | Change as demand |
| $d_1$, $d_2$ | Depth of the wedge-shaped basin model on two sides | Change as demand |
| $w$ | Width of the mountain | 3000 m |
| $V_p$ | Compression wave velocity | Change as demand |
| $V_s$ | Shear wave velocity | Change as demand |
| $\rho$ | Density | Change as demand |
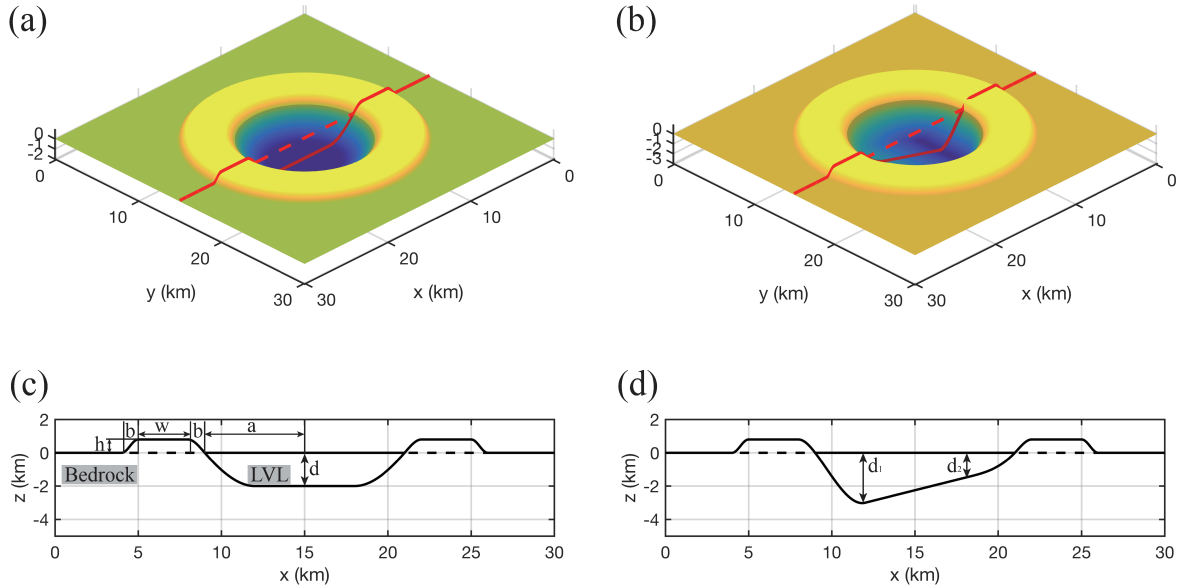
**Fig. 1.** Basin model geometry. Three-dimensional basin geometry for the (a) fixed-depth basin model and (b) wedge-shaped basin model, where the subsurface concave regions are filled with low-velocity media. The cross-sections of the central red lines in (a) and (c) are shown in (c) and (d). The geometric parameters of the basin are labeled in (c) and (d), whose definitions are listed in Table 1. In the following ground surface images in this study, the geometric cross-section of the basin is depicted in the center of the images.

(points per minimum wavelength) of 8, the wave field can provide a reliable frequency of up to 3.75 Hz. The size of the model is 30 km × 30 km × 12 km, and the grid points within the simulation area are 600 × 600 × 90. A total of 144 cores in a cluster are used for the simulation.

### 2.3 Ground motion amplification evaluation

The ground motion amplification is characterized by peak ground velocity (PGV), peak ground acceleration (PGA), and amplification factor. Regarding the amplification factor, we followed the approach of Wirth et al.[14] with modifications to achieve a smoother graphical representation. The following procedure is applied to calculate the amplification factor on the ground surface: Start with the low-pass filtered velocity seismogram at each grid point $v(t; x, y)$, we perform a Fourier transform on the filtered waveform to obtain the amplitude spectrum $F(\omega; x, y) = \mathcal{F}[v(t; x, y)]$. The reference model's ground motion is calculated with a half-space homogeneous model, whose amplitude spectrum $F_{ref}(\omega; x, y) = \mathcal{F}[v_{ref}(t; x, y)]$ is also calculated. The amplification factor $\gamma$ is defined as

$$\gamma(x, y) = \frac{\max[F(\omega; x, y)]}{\max[F_{ref}(\omega; x, y)]}. \tag{3}$$

For each grid point, we can obtain the amplification factor $\gamma(x, y)$ and the corresponding $\omega_{max}$. Through this method, we can obtain spectral ratios of basin amplification relative to the reference model. By dividing the maximum of the reference model amplitude spectrum, we can eliminate the effects of source radiation patterns and geometric spreading, allowing for a more accurate evaluation of the influences of topography and low-velocity layers on ground motion. This helps to minimize the effect of single-station local errors and to find the maximum amplification among different frequencies[39]. The amplification factor in this work is calculated using the vertical (z-component) velocity seismogram.

The reason for modifying the approach of Wirth et al.[14] is that, in models with sharp velocity boundaries, the results obtained through comparing amplitude spectra at a fixed frequency exhibit spatial discontinuities. A comparison of the maximum values of the amplitude spectra provides a smoother representation of the model. Due to variations in model and seismic source configurations across different studies, the amplification factor obtained through this method can only be compared within the scope of this study. The results are internally consistent and can reflect the amplification characteristics.

## 3 Results

### 3.1 Overall characteristics of ground motion

To understand the effect of the low-velocity layer on ground motion amplification, we filled the basin area with low-velocity material. This baseline model LVL has a $V_s$ velocity of 1500 m/s, whereas bedrock has a $V_s$ velocity of 3000 m/s, with all other parameters constant with the baseline parameter. We apply a simple dislocation source at (9000 m, −15000 m, −1000 m). The moment is 1.23e18 Nm, corresponding to ~Mw 6.0. For the source, the strike dip and rake are 0 degrees, 45 degrees, and 90 degrees, respectively. In subsequent simulations, we applied the same source configuration. The velocity seismograms on the ground are subjected to a low-pass filter with a cutoff frequency of 3.75 Hz, and the amplification factor is subsequently calculated.

A source time function of the Ricker wavelet is applied with a central frequency $f_c$ of 2 Hz and a time shift $t_0$ of 0.7 s. With a basin depth $d$ of 1000 m, the ground motion snapshot is shown in Fig. 2. The results show that the seismic waves keep oscillating inside the basin area, especially near the boundary area. Upon reaching the far end of the basin, seis-
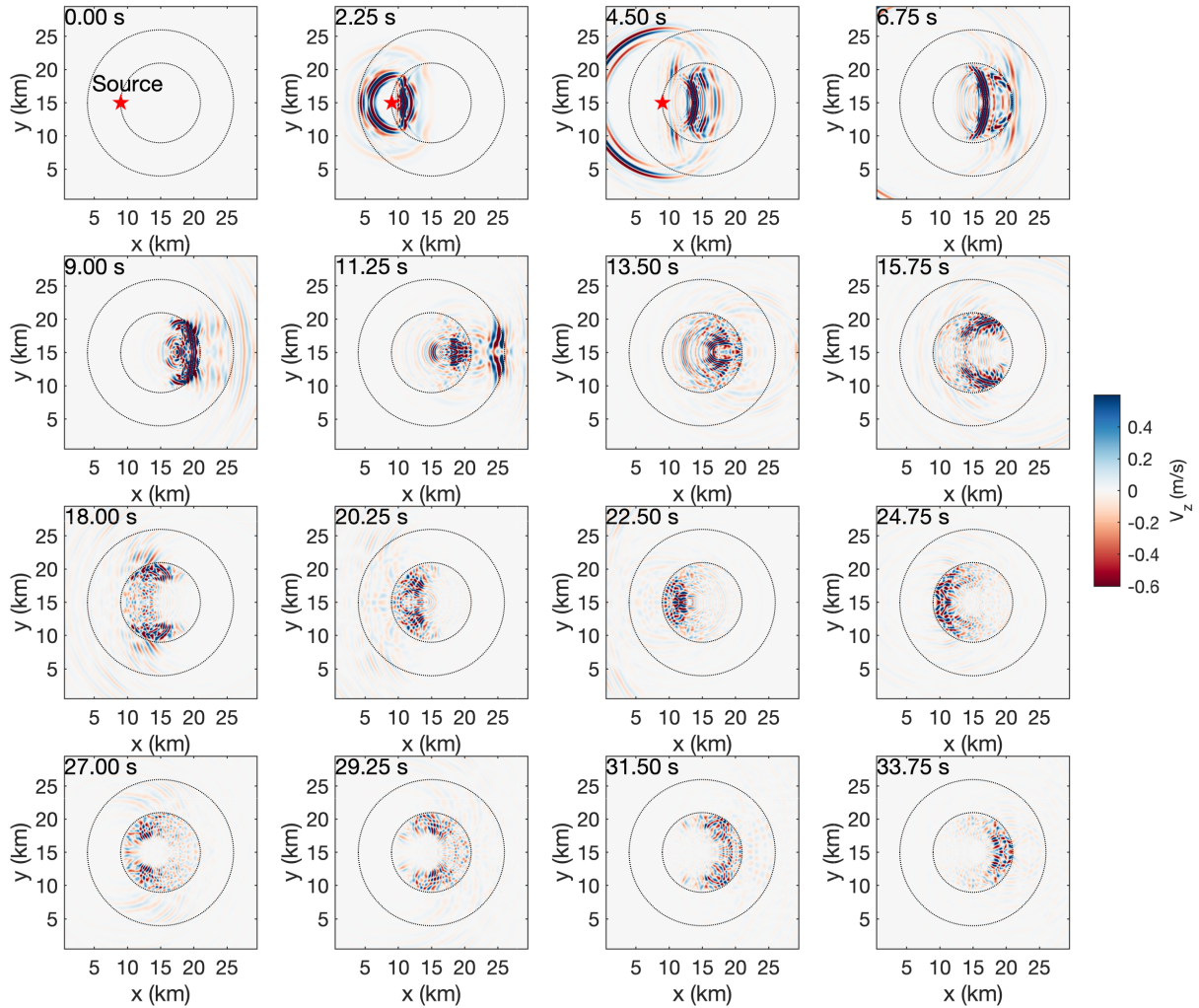
**Fig. 2.** Z-component velocity snapshot at the ground surface of the fixed-depth baseline model.

mic waves reflect due to velocity contrasts and return to the interior part of the basin. This oscillatory process repeats continuously, resulting in a larger amplitude and longer duration of ground motion within the low-velocity region.

The distribution of the maximum PGVz and PGVh values (Fig. 3a, 3b) is related to the radiation pattern of the reverse fault dislocation source we applied. As shown in Fig. 3a, the amplification extends in a V-shaped pattern within the basin. On the west side of the source, the V-shaped pattern is obstructed by the topography and has a narrower distribution than the east side, which is covered by the LVL. On the western edge of the mountain range, ground motion amplification caused by changes in topography can be observed, mainly on the boundary of the mountain. A more distinct block-like distribution is observed in PGVh than in PGVz (Fig. 3b). Compared with the distribution of the PGV, the distribution of the amplification factor can illustrate the boundary of the LVL. In this baseline model, regions with stronger amplification are present in the middle of the basin (Fig. 3c). Fig. 4a shows the 3-component seismogram at receiver line 1, and a Z-shaped pattern of repetitive ground motion can be observed. Because the central part between the red lines of line 1 is located within the low-velocity region, their intensity is significantly

greater than that of the receivers outside the basin. Fig. 4b shows the 3-component seismograms at receiver line 2. The strongest amplification occurs a few seconds after the seismic wave enters the basin; however, the oscillation inside the basin can persist for an extended period, especially near the basin boundary. In contrast, the oscillation is weaker at the center of the basin.

## 3.2　Effect of the LVL depth

To understand the effect of the low-velocity layer on ground motion amplification, we filled the basin area with low-velocity material. With all other parameters constant with the baseline parameter, we investigate three different scenarios, with the basin depth $d$ changing from 1000 m to 2000 m with an interval of 500 m. The seismic source configuration is the same as that in the previous section.

The amplification factor reveals stronger amplification within the LVL zone, especially within the flat area of the LVL (Fig. 5a, 5b, 5c). Compared with the half-space homogeneous reference model, the basin has two regions with more pronounced amplification values within the LVL zone. The first peak is located in the transitional zone between the flat and slope parts of the basin and represents a circle close to the source. This is related to the pattern of the homogen-
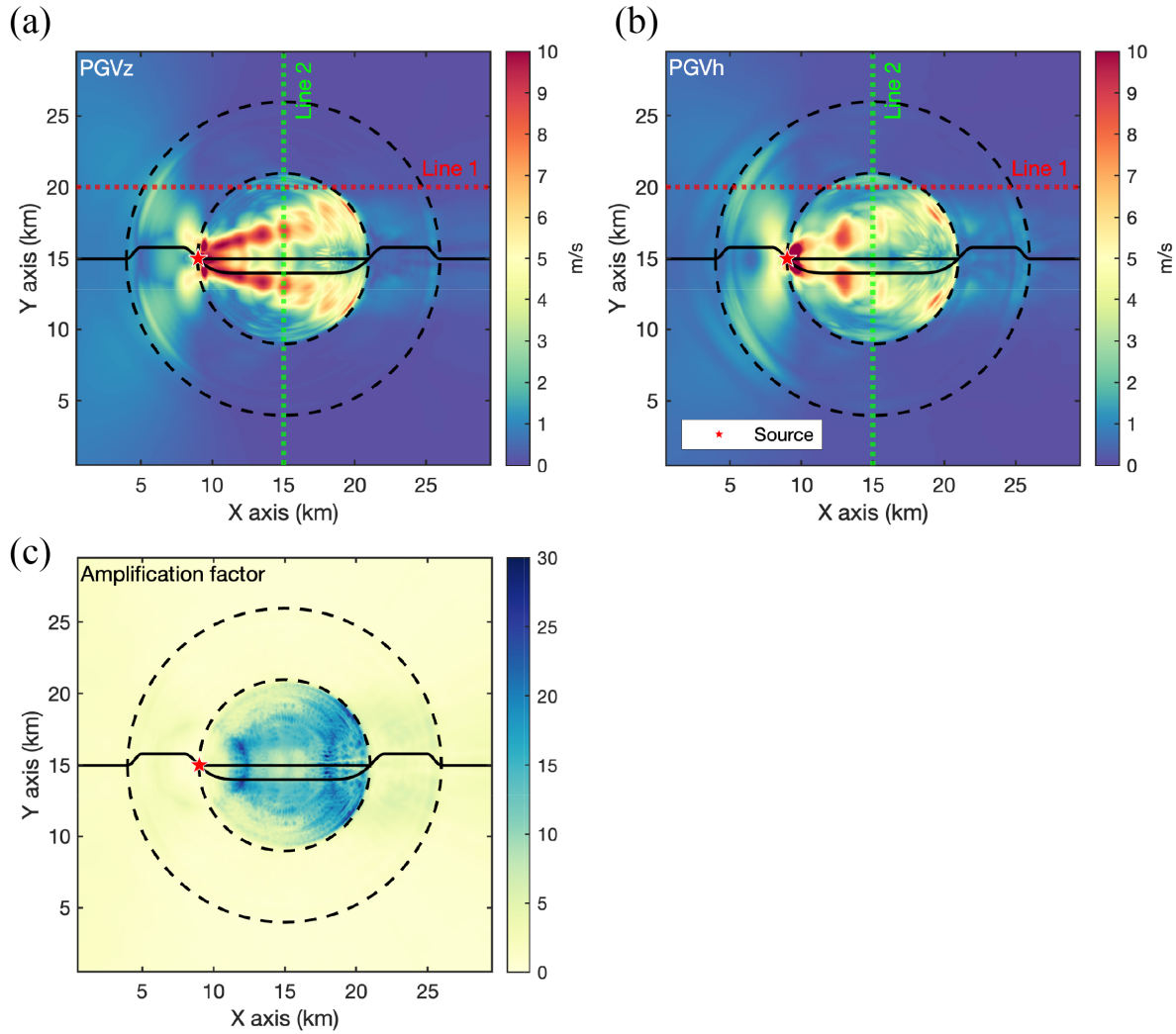
(a)

(b)

(c)

**Fig. 3.** (a) PGVz, (b) PGVh, and (c) amplification factor of the fixed-depth baseline model at the ground surface. In (a), (b), and (c), the dashed circle shows the boundary of the LVL and topography. The central section profile is drawn in the center of the plot with a solid black line. The dashed red line and green line in (a) and (b) represent two lines of receivers.

eous half-space model reference result used to calculate the amplification factor. Additionally, amplification primarily occurs on the far side of the basin, with an amplification factor of 20 to 30 compared with that of the reference model.

The maximum PGV values decrease with increasing LVL depth (Fig. 5d, 5e, 5f). The number of PGV local peaks within the basin area decreases from 4 groups to 1 group as the basin depth increases from 1000 m to 2000 m. This phenomenon may indicate a reduction in the number of multiple reflections within the basin. Thus, we infer that basin depth is not the primary factor influencing the degree of amplification within the basin but does alter the distribution pattern of amplification within the basin.

### 3.3 Effect of the LVL velocity

The shear wave velocity of the bedrock below the basin topography is 3000 m/s. By changing the medium velocity within the sediment basin from 1500 m/s to 3000 m/s with an interval of 500 m/s, we investigate 4 different scenario cases and show the amplification factor and PGVz in Fig. 6. Generally, the absence of the LVL controls the amplification behavior.

The strongest amplification without the source area occurs at the far end of the basin. The magnitude of the velocity contrast directly controls the magnitude of the amplification factor. As the LVL velocity increases, the amplification decreases. A velocity contrast of 1500 m/s leads to a maximum amplification factor of ~30.

Apart from the significant amplification of ground motion within the basin, the basin acts as a kind of "lens", causing waves to focus as they pass through the basin, resulting in a V-shaped pattern of increased ground motion that persists beyond the LVL zone. This finding demonstrates that the energy originating from the source is still more concentrated than that of the reference model even after passing through the basin. As the velocity contrast diminishes, this phenomenon of wavefront focusing weakens, and the opening of the V-shape gradually widens until it disappears.

As the velocity contrast diminishes, the locations with stronger amplification within the basin shift from the central flat region of the basin to areas on either side of the basin. The central region of the basin exhibits a greater peak when
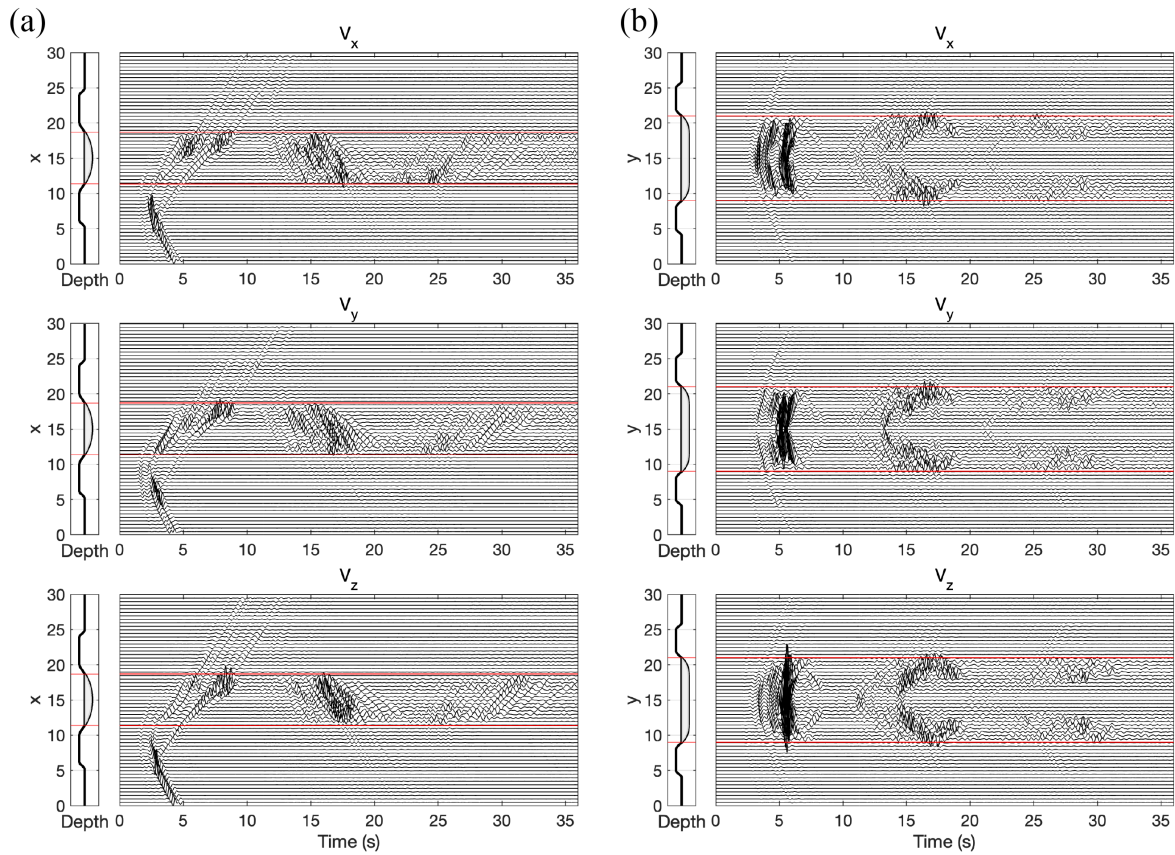
**Fig. 4.** 2D section of the model geometry and corresponding 3-component velocity seismograms for (a) receiver line 1 and (b) receiver line 2 in Fig. 3a with the fixed-depth baseline model.
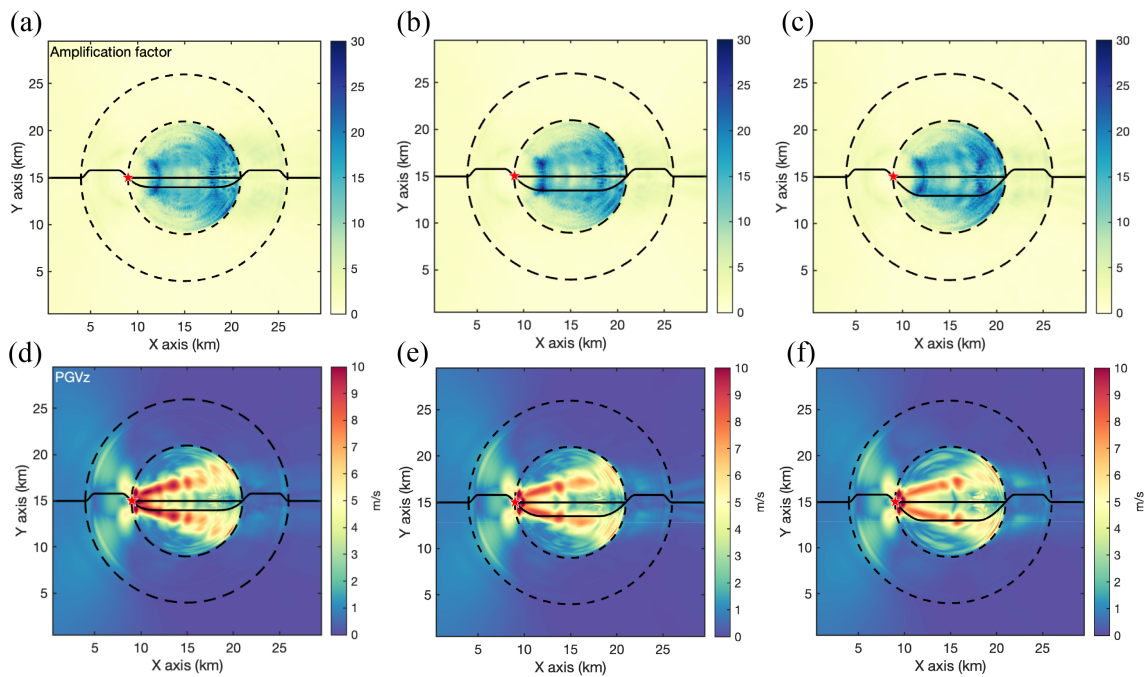


**Fig. 5.** Amplification factor of the fixed-depth basin model with LVL depths of (a) 1000 m, (b) 1500 m, and (c) 2000 m and the corresponding vertical PGV (d), (e), and (f). The dashed circle shows the boundary of the LVL and topography.
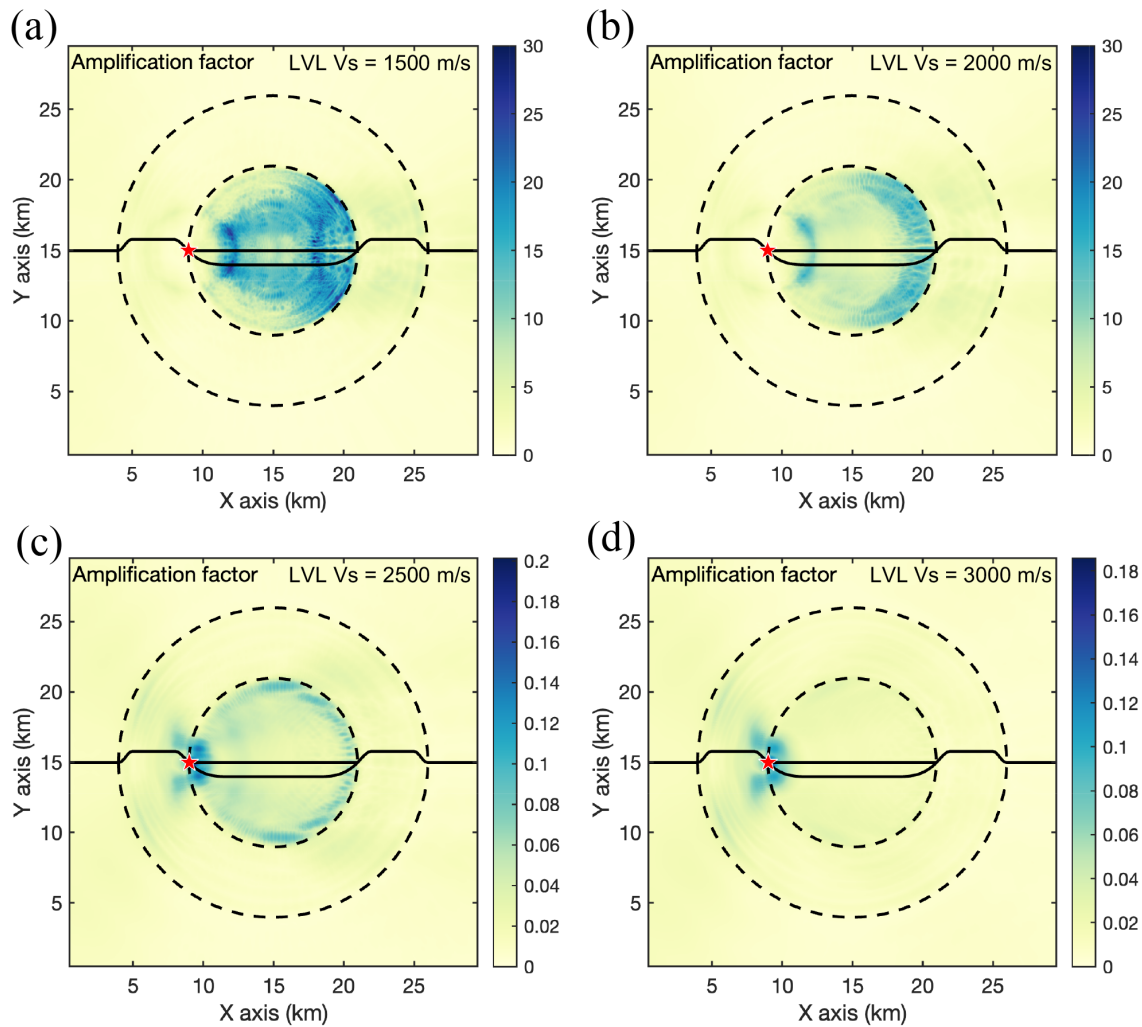
**Fig. 6.** Amplification factor of fixed-depth basin model with LVL velocities of (a) 1500 m/s, (b) 2000 m/s, (c) 2500 m/s, and (d) 3000 m/s, with a velocity of 3000 m/s of the bedrock.

the first arrivals of waves reach it, and the level of amplification depends on the strength of the transmitted and reflected waves upon their initial entry into the basin. However, reflected waves on the opposite side of the basin primarily propagate back and forth around the perimeter of the basin, possibly because of the thinner transitional zones around the periphery, resulting in more pronounced multiple reflections. As the velocity contrast varies, there is a change in the balance between the first arrivals and subsequent multiple reflections in the amplification components. In Fig. 6d, there is no velocity contrast in this model, the amplification is caused only by tomography.

## 4 Discussion

Near-field ground motion amplification in basin areas has been the subject of extensive research through numerous 2D and 3D studies. However, in areas associated with sedimentary faults, the gradual rotation and subsidence of the fault's down-dropped block create additional space near the fault, allowing for the deposition of thicker sedimentary layers. This

process disrupts the sedimentary symmetry and leads to the formation of wedge-shaped sedimentary layers, which are commonly observed in basin-rift structure regions[40]. The fault is typically located at the deeper end of the fault. To address this gap, we constructed a wedge-shaped basin model parameterized by $d_1$ and $d_2$ (Fig. 1d). To maintain consistency in the model set-up, we retained the same seismic source configuration as in the previous model. In such a model configuration, we obtained the results as shown in Fig. 7. $d_1 = 3000$ m and $d_2 = 1500$ m are applied in this case, whose definitions are described in Fig. 1d.

For a model with a wedge-shaped LVL, the general characteristics of wave propagation are similar to those of a fixed-depth basin model. Strong amplification still occurs at the far end of the basin compared with the other models. The model results also differ somewhat from compared to the previous results with a fixed basin depth. According to the PGV distribution (Fig. 7a), the V-shaped feature within the basin area exhibits a more extended reach due to the basin, continuing into the transitional zone where it converges toward the ground at the far side of the basin. Its distribution is more
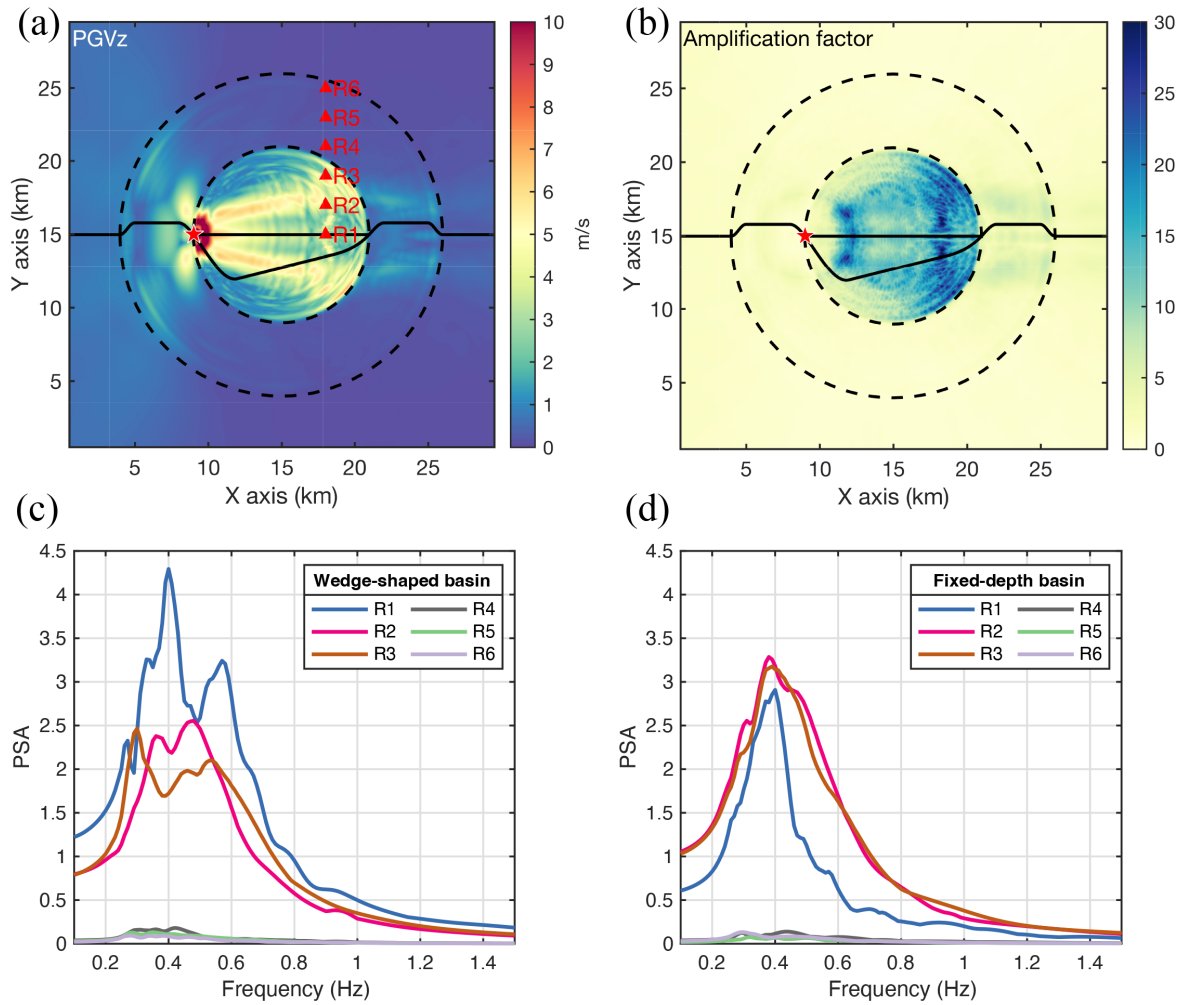
**Fig. 7.** (a) PGVz for the wedge-shaped LVL model. (b) z-component amplification factor of the wedged-shaped LVL model. (c) PSA with a 5% damping ratio of the wedge-shaped model at the receivers in Fig. 7a. (d) PSA with a 5% damping ratio of the 1500 m fixed-depth basin model at the corresponding receivers.

continuous than that of a fixed-depth basin model. In terms of the amplification factor (Fig. 7b), the amplification factor on the shallower side of the basin is greater than that on the corresponding position in the fixed-depth basin model. This discrepancy may be attributed to the fact that once waves enter the basin, the larger angle between the basin's bottom boundary and the wavefront weakens the multiple reflections of waves within the LVL. As the basin depth gradually becomes shallower, stronger amplification occurs at the far end of the basin.

We compare the PSA of the 6 receivers, indicated by the red triangles in Fig. 7a, between the wedge-shaped model and the 1500 m fixed-depth model (Fig. 7c and 7d). Among these 6 receivers, receivers R4, R5, and R6 are located outside the basin area. The PSA at R2 and R3 of the wedge-shaped model are truncated and exhibit a transition from a single-peak distribution in the fixed-depth basin model to a double-peak distribution compared with those the fixed-depth model. The PSA of R1 in the wedged-shape model has a larger peak than that in the fixed-depth model. The difference at R1 indicates that under the wedge-shaped basin, owing to variations in the

reflection characteristics on the boundary of the LVL, the amplification pattern differs from that of a fixed-depth basin. This illustrates the effects of basin geometry on the response of structures to ground motion. Furthermore, compared with receivers outside the basin, the PSA peaks of receivers within the LVL zone have slightly shifted toward higher frequencies. The PSA at receivers outside the LVL zone are nearly identical between the two models.

The wedge-shaped model is x-axis symmetric, and the z-component PGV and the amplification factor both have smaller values at the symmetry axis compared to the maximum of the area. Although back-and-forth oscillations of seismic waves occur on the opposite sides of the basin, their ground motion at this location is weaker than that of its surroundings. This highlights the significance of model configuration for different ground motion characteristics. Compared with the influence of the LVL effect, the influence of topography on ground motion is secondary, which coincides with previous studies[23,41]. The amplification due to topography primarily occurs at locations where there are variations in the terrain, which is notably evident at the edge of the western mountain

range in Fig. 6d.

The current configuration places a seismic source near the outer boundary between the LVL and the underlying bedrock under the assumption that a basin-rift structure can generate faults at the boundary. However, large earthquakes can also originate on faults adjacent to the basin. To investigate the impact of source location, we conducted additional tests with two different source positions outside the basin. Fig. 8 presents a comparison of the maximum amplification factor and z-component velocity snapshots for three different source locations, S1, S2, and S3. The simulation region is extended to 40 km × 30 km × 12 km to adjust the change in source locations. The same focal mechanism and source depth are used. The x-axis coordinates of Source S1 remain at 9000 m, which is consistent with earlier models. However, for Source S2, we shifted its x-axis coordinate to 6500 m, placing it beneath the center of the surrounding mountains. Source S3 is moved further away from the mountain area, with its x-axis coordinate at 0 m. The basin depth is 2000 m, and the LVL $V_s$ velocity is 1500 m/s, whereas the bedrock $V_s$ velocity is 3000 m/s.

The maximum amplification factor exhibits noticeable differences for different source locations, S1, S2, and S3 (Fig. 8a, 8c, 8e). As the distance between the source and the LVL increases, the maximum amplification factor decreases. This outcome is not surprising for two main reasons. First, the energy entering the LVL diminishes with increasing distance because of attenuation and geometrical spreading. Second,

considering a source depth of 1000 m and an LVL depth of 2000 m, waves entering the basin at greater distances exhibit a nearly perpendicular wavefront orientation to the Earth's surface, resulting in a reduction in multiple reflections within the LVL.

The results with different source distances consistently indicate a shift in the maximum amplification toward the far side of the basin from the source. To better understand this phenomenon, we present the z-component velocity snapshots in Fig. 8b, 8d, and 8f. The travel times from the source to the LVL for source models S1, S2, and S3 are approximately 0 s, 4.8 s, and 5.73 s, respectively. Thus, we choose the snapshot time at 4 s and 15 s after the wavefront reaches the LVL. For source models S1 and S2, the reflection of seismic waves induced by the mountain is observed. This reflected wave, upon entering the LVL, amplifies the amplitude and prolongs the duration of the ground motion within the LVL. For source model S2, seismic waves are trapped for a longer time because of free-surface reflection. This leads to a larger amplification factor almost everywhere on the outside slope of the surrounding mountain. This finding aligns with previous research, both analytical and numerical, indicating that the amplification caused by mountain topography typically occurs on mountain ridges or slopes[23,33,41–43]. While the source is outside of the mountain region, the reflection of the seismic wave amplitude is too subtle to discern. Nevertheless, once the wavefronts enter the basin area, they can still be trapped in
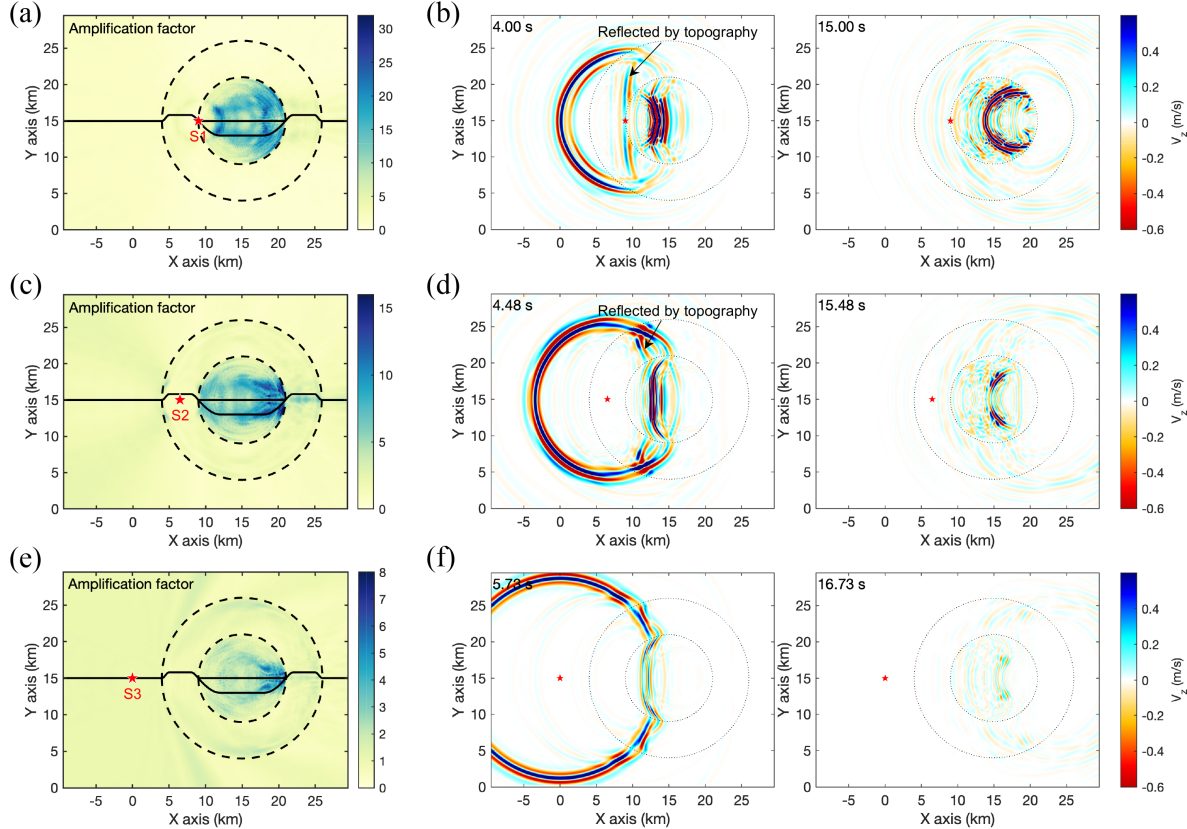


**Fig. 8.** Amplification factor with different source locations (a, c, e) and corresponding z-component velocity snapshots at 4 s and 15 s after the wavefront reaches the LVL (b, d, f). The result is calculated via a fixed-depth basin model.

the basin area and amplify the ground motion, although the amplitude is weaker than that of previous models.

# 5  Conclusions

Scrutinizing the basin amplification effect is crucial to earthquake hazard assessment. To address the gap in the coupling effect of basin topography and the low-velocity layer, we design several different basin models generated using a combination of a half-sine function and cubic spline interpolation, each with varying low-velocity sediments. We then simulate seismic wave propagation through these models using finite difference method. Comparative analysis with results from a homogeneous half-space model allowed us to assess the influence of the low-velocity layer and topography on ground motion. Compared with the effect of basin topography, which is concentrated mainly in the enclosing mountain area near the side facing toward the seismic source, the low-velocity layer effect is more crucial for determining ground motion amplification. With a greater velocity contrast between the LVL and the bedrock, stronger seismic amplification mainly appears in the central flat region of the basin and is more pronounced on the side of the basin opposite the seismic source. With a lower velocity contrast, ground motion amplification primarily occurs in the periphery part of the basin. In addition to the fixed-depth basin model, we also propose a wedge-shaped basin model, which is common in rift-basin structures, and compare the differences in the PSA of the wedge-shaped and fixed-depth basin models. A stronger PSA is observed at points closer to the central line of the basin. The distance between the source and the basin, coupled with the basin boundary topography, can strongly affect ground motion amplification. Our work provides useful insight into understanding basin amplification patterns and helps explain near-field ground motion with various basin characteristics. This study also highlights the importance of both velocity structure and topography in seismic hazard assessments. The realistic complex topography in basin areas surrounded by mountains, such as the Los Angeles and Sichuan Basins, may induce more intricate coupling effects between topography and basin structure, warranting further investigation in future studies.

# Acknowledgements

# Conflict of interest

The authors declare that they have no conflict of interest.

# Biographies

**Zeyu Lu**   is a master's student at the University of Science and Technology of China. He received his bachelor's degree in Geophysics from China University of Geosciences (Beijing) in 2022. His research mainly focuses on the earthquake dynamic rupture process and earthquake ground motion simulation.

**Feng Hu**   is an Associate Professor at the University of Science and Technology of China (USTC). He received his Ph.D. degree in Geophysics at USTC in 2014. His research mainly focuses on rupture dynamics, earthquake hazard simulations, and seismicity analysis.

# References

[1] Pitarka A, Irikura K, Iwata T, et al. Three-dimensional simulation of the near-fault ground motion for the 1995 Hyogo-Ken Nanbu (Kobe), Japan, earthquake. *Bulletin of the Seismological Society of America*, **1998**, *88* (2): 428–440.

[2] Yu Z, Liu Q, Xu J, et al. Simulation of dynamic rupture process and near-field strong ground motion for the Wenchuan earthquake. *Bulletin of the Seismological Society of America*, **2022**, *112* (6): 2828–2846.

[3] Graves R W. Preliminary analysis of long-period basin response in the Los Angeles region from the 1994 Northridge earthquake. *Geophysical Research Letters*, **1995**, *22* (2): 101–104.

[4] Xu W, Wu P, Li D, et al. Joint inversion of Rayleigh group and phase velocities for S-wave velocity structure of the 2021 Ms 6.0 Luxian earthquake source area, China. *Earthquake Science*, **2023**, *36* (5): 356–375.

[5] Zhao Y, Jiang G, Lei X, et al. The 2021 Ms 6.0 Luxian (China) earthquake: Blind reverse-fault rupture in deep sedimentary formations likely induced by pressure perturbation from hydraulic fracturing. *Geophysical Research Letters*, **2023**, *50* (7): e2023GL103209.

[6] Bard P-Y, Bouchon M. The seismic response of sediment-filled valleys. Part 2. The case of incident P and SV waves. *Bulletin of the Seismological Society of America*, **1980**, *70* (5): 1921–1941.

[7] Dravinski M. Influence of interface depth upon strong ground motion. *Bulletin of the Seismological Society of America*, **1982**, *72* (2): 597–614.

[8] Dravinski M, Mossessian T K. Scattering of plane harmonic P, SV, and Rayleigh waves by dipping layers of arbitrary shape. *Bulletin of the Seismological Society of America*, **1987**, *77* (1): 212–235.

[9] Ayoubi P, Mohammadi K, Asimaki D. A systematic analysis of basin effects on surface ground motion. *Soil Dynamics and Earthquake Engineering*, **2021**, *141*: 106490.

[10] Kamal, Narayan J P. 3D basin-shape ratio effects on frequency content and spectral amplitudes of basin-generated surface waves and associated spatial ground motion amplification and differential ground motion. *Journal of Seismology*, **2015**, *19* (2): 293–316.

[11] Qin Y, Wang Y, Takenaka H, et al. Seismic ground motion amplification in a 3D sedimentary basin: the effect of the vertical velocity gradient. *Journal of Geophysics and Engineering*, **2012**, *9* (6): 761–772.

[12] Liu Z X, Huang Z E, Zhang Z, et al. Three-dimensional preconditioned FM-IBEM solution to broadband-frequency seismic wave scattering in a layered sedimentary basin. *Engineering Analysis with Boundary Elements*, **2021**, *133*: 1–18.

[13] Liu Z X, Huang Z E, Meng S B. Three-dimensional IBEM solution to seismic wave scattering by a near-fault sedimentary basin. *Engineering Analysis with Boundary Elements*, **2022**, *140*: 220–242.

[14] Wirth E A, Vidale J E, Frankel A D, et al. Source-dependent amplification of earthquake ground motions in deep sedimentary basins. *Geophysical Research Letters*, **2019**, *46* (12): 6443–6450.

[15] Frankel A, Stephenson W, Carver D. Sedimentary basin effects in Seattle, Washington: Ground-motion observations and 3D simulations. *Bulletin of the Seismological Society of America*, **2009**,

99 (3): 1579–1611.

[16] Frankel A D, Carver D L, Williams R A. Nonlinear and linear site response and basin effects in Seattle for the M 6.8 Nisqually, Washington, earthquake. *Bulletin of the Seismological Society of America*, **2002**, *92* (6): 2090–2109.

[17] Jayalakshmi S, Dhanya J, Raghukanth S T G, et al. 3D seismic wave amplification in the Indo-Gangetic basin from spectral element simulations. *Soil Dynamics and Earthquake Engineering*, **2020**, *129*: 105923.

[18] Esmaeilzadeh A, Motazedian D. Sensitivity analysis for finite-difference seismic basin modeling: A case study for Kinburn basin, Ottawa, Canada. *Bulletin of the Seismological Society of America*, **2019**, *109* (6): 2305–2324.

[19] Fu C, Gao M, Chen K. A study on long-period response spectrum of ground motion affected by basin structure of Beijing. *Acta Seismologica Sinica*, **2012**, *34* (03): 374–382. (in Chinese)

[20] Lee S-J, Chen H-W, Huang B-S. Simulations of strong ground motion and 3D amplification effect in the Taipei basin by using a composite grid finite-difference method. *Bulletin of the Seismological Society of America*, **2008**, *98* (3): 1229–1242.

[21] Miksat J, Wen K-L, Sokolov V, et al. Simulating the Taipei basin response by numerical modeling of wave propagation. *Bulletin of Earthquake Engineering*, **2010**, *8* (4): 847–858.

[22] Sokolov V, Wen K-L, Miksat J, et al. Analysis of Taipei basin response for earthquakes of various depths and locations using empirical data. *Terrestrial, Atmospheric and Oceanic Sciences: TAO*, **2009**, *20* (5): 687–702.

[23] Boore D M. A note on the effect of simple topography on seismic SH waves. *Bulletin of the Seismological Society of America*, **1972**, *62* (1): 275–284.

[24] Bouchon M. Effect of topography on surface motion. *Bulletin of the Seismological Society of America*, **1973**, *63* (2): 615–632.

[25] Davis L L, West L R. Observed effects of topography on ground motion. *Bulletin of the Seismological Society of America*, **1973**, *63* (1): 283–298.

[26] Çelebi M. Topographical and geological amplifications determined from strong-motion and aftershock records of the 3 March 1985 Chile earthquake. *Bulletin of the Seismological Society of America*, **1987**, *77* (4): 1147–1167.

[27] Geli L, Bard P-Y, Jullien B. The effect of topography on earthquake ground motion: A review and new results. *Bulletin of the Seismological Society of America*, **1988**, *78* (1): 42–63.

[28] Bourdeau C, Havenith H B. Site effects modelling applied to the slope affected by the Suusamyr earthquake (Kyrgyzstan, 1992). *Engineering Geology*, **2008**, *97* (3): 126–145.

[29] Rizzitano S, Cascone E, Biondi G. Coupling of topographic and stratigraphic effects on seismic response of slopes through 2D linear and equivalent linear analyses. *Soil Dynamics and Earthquake Engineering*, **2014**, *67*: 66–84.

[30] Luo Y, Fan X, Huang R, et al. Topographic and near-surface stratigraphic amplification of the seismic response of a mountain slope revealed by field monitoring and numerical simulations. *Engineering Geology*, **2020**, *271*: 105607.

[31] Huang D, Sun P, Jin F, et al. Topographic amplification of ground motions incorporating uncertainty in subsurface soils with extensive geological borehole data. *Soil Dynamics and Earthquake Engineering*, **2021**, *141*: 106441.

[32] Wang G, Du C Y, Huang D R, et al. Parametric models for 3D topographic amplification of ground motions considering subsurface soils. *Soil Dynamics and Earthquake Engineering*, **2018**, *115*: 41–54.

[33] Hailemikael S, Lenti L, Martino S, et al. Ground-motion amplification at the Colle di Roio ridge, central Italy: a combined effect of stratigraphy and topography. *Geophysical Journal International*, **2016**, *206* (1): 1–18.

[34] Zhang W, Zhang Z, Chen X. Three-dimensional elastic wave numerical modelling in the presence of surface topography by a collocated-grid finite-difference method on curvilinear grids. *Geophysical Journal International*, **2012**, *190* (1): 358–378.

[35] Hixon R. On increasing the accuracy of MacCormack schemes for aeroacoustic applications. In: 3rd AIAA/CEAS Aeroacoustics Conference. Reston, VA, USA: American Institute of Aeronautics and Astronautics, **1997**.

[36] Chen X, Quan Y, Harris J M. Seismogram synthesis for radially layered media using the generalized reflection/transmission coefficients method: Theory and applications to acoustic logging. *Geophysics*, **1996**, *61* (4): 1150–1159.

[37] Komatitsch D, Tromp J. Introduction to the spectral element method for three-dimensional seismic wave propagation. *Geophysical Journal International*, **1999**, *139* (3): 806–822.

[38] Brocher T M. Empirical relations between elastic wavespeeds and density in the Earth's crust. *Bulletin of the Seismological Society of America*, **2005**, *95* (6): 2081–2092.

[39] Wirth E A, Chang S W, Frankel A. 2018 report on incorporating sedimentary basin response into the design of tall buildings in Seattle, Washington. Reston, VA, USA: U.S. Geological Survey, **2018**: Open-File Report 2018-1149.

[40] Withjack M O, Schlische R W, Olsen P E, et al. Rift-basin structure and its influence on sedimentary systems. In: Sedimentation in Continental Rifts. Claremore, OK, USA: Society for Sedimentary Geology, **2002**: 57–81.

[41] Graizer V. Low-velocity zone and topography as a source of site amplification effect on Tarzana hill, California. *Soil Dynamics and Earthquake Engineering*, **2009**, *29* (2): 324–332.

[42] García-Pérez T, Ferreira A M G, Yáñez G, et al. Effects of topography and basins on seismic wave amplification: the Northern Chile coastal cliff and intramountainous basins. *Geophysical Journal International*, **2021**, *227* (2): 1143–1167.

[43] Lee S-J, Chan Y-C, Komatitsch D, et al. Effects of realistic surface topography on seismic ground motion in the Yangminshan region of Taiwan based upon the spectral-element method and LiDAR DTM. *Bulletin of the Seismological Society of America*, **2009**, *99* (2A): 681–693.